European Journal of Medicinal Chemistry 227 (2022) 113932

Contents lists available at ScienceDirect

European Journal of Medicinal Chemistry

journal homepage: http://www.elsevier.com/locate/ejmech

# Exploring disordered loops in DprE1 provides a functional site to combat drug-resistance in *Mycobacterium* strains

Jiyuan Liu [a, 1], Huanqin Dai [b, c, 1], Bo Wang [b, d], Hongwei Liu [b, c, **], Zhen Tian [a, ***], Yalin Zhang [a, *]

[a] Key Laboratory of Plant Protection Resources & Pest Management of the Ministry of Education, College of Plant Protection, Northwest A&F University, Yangling, 712100, Shaanxi, China
[b] State Key Laboratory of Mycology, Institute of Microbiology, Chinese Academy of Sciences, No.1 Beichenxi Road, Chaoyang District, Beijing, 100101, China
[c] Savaid Medical School, University of Chinese Academy of Sciences, Beijing, 100049, China
[d] Health Service Department of PLA General Hospital, No.28 Fuxing Road, Beijing, 100864, China

ARTICLE INFO

*Article history:*
Received 17 August 2021
Received in revised form
30 September 2021
Accepted 15 October 2021
Available online 20 October 2021

*Keywords:*
Tuberculosis
Drug resistance
DprE1
Flexible loops
Drug optimization
Cyclopropyl
Benzothiazole
Electrostatic complementarity

ABSTRACT

As an anti-tuberculosis target, DprE1 contains two flexible loops (Loop I and Loop II) which have never been exploited for developing DprE1 inhibitors. Here Leu317 in Loop II was discovered as a new functional site to combat drug-resistance in *Mycobacterium* strains. Based on TCA1, LZDT1 was designed to optimize the hydrophobic interaction with Leu317. A subsequent biochemical and cellular assay displayed increased potency of LZDT1 in inhibiting DprE1 and killing drug-sensitive/-resistant *Mycobacterium* strains. The improved activity of LZDT1 and its analogue LZDT2 against multidrug resistant tuberculosis was particularly highlighted. For LZDT1, its enhanced interaction with Leu317 also impaired the drug-insensitivity of DprE1 caused by Cys387 mutation. A new nonbenzothiazole lead (LZDT10) with reduced Cys387-dependence was further produced by optimizing interactions with Leu317, improvement directions for LZDT10 were discussed as well. Our research underscores the value of potential functional sites in disordered loops, and affords a feasible way to develop these functional sites into opportunities for drug-resistance management.



## 1. Introduction

Tuberculosis (TB) remains a leading cause of human mortality worldwide. Its global epidemic is, at least in part, exacerbated by the alarming rise of drug resistant TB (DR-TB) [1,2]. The high prevalence of DR-TB could greatly hamper current treatments for TB, resulting in higher failure rates, longer treatment time, and more complicated drug regimens [3]. Currently, the chemotherapy of TB consists of three lines of therapeutic regimen. Nevertheless, treatment of DR-TB can extend up to 2 years. Such a lengthy process, along with associated side-effects, often cause premature non-compliance by patients, exacerbating the problem of drug resistance [2,3]. More seriously, the current COVID-19 pandemic could cause severe reductions in timely diagnosis and treatment of new TB cases, further increasing TB burden [4–7]. In combatting TB today, the lack of newer and more efficacious drugs is a serious problem [3,8,9]. Since the approval of rifampin (RIF) in the 1960s, only two new anti-TB drugs (bedaquiline and pretomanid) have been approved by FDA. Much effort continues to be directed towards discovering new anti-TB drugs [10–16].

Decaprenylphosphoryl-β-D-ribofuranose 2-oxidase (DprE1) has been proposed as a vulnerable anti-TB target, due to its periplasm location and essential role in forming the mycobacterial cell wall [17–19]. Inhibitors for DprE1 have the potential of providing future drug candidates for resolving the DR-TB crisis [19–22]. To date, multiple compounds act as either covalent or non-covalent DprE1 inhibitors with anti-mycobacterial activity have been identified [23]. Among these, a benzothiazole derivative TCA1 is particularly highlighted by its inhibitory property against the active

* Corresponding author.
** Corresponding author. State Key Laboratory of Mycology, Institute of Microbiology, Chinese Academy of Sciences, No.1 Beichenxi Road, Chaoyang District, Beijing, 100101, China.
*** Corresponding author.
*E-mail addresses:* liuhw@im.ac.cn (H. Liu), tianzhen@nwsuaf.edu.cn (Z. Tian), yalinzh@nwsuaf.edu.cn (Y. Zhang).
[1] J.Y.L. and H.Q.D. contributed equally to this work.

https://doi.org/10.1016/j.ejmech.2021.113932
0223-5234/

(replicating) and latent (nonreplicating) *Mycobacterium tuberculosis* (*Mtb*). In addition, TCA1 is verified to be efficacious in acute and chronic rodent models of TB [24]. The compound is therefore considered a promising lead compound. Guided by the crystal structure of DprE1 in complex with TCA1 (PDB ID: 4KW5), significant optimizations have been made, decreasing the minimum inhibitory concentration (MIC) from 0.23 μM for TCA1 to 0.089 μM for TCA007 and 0.046 μM for TCA481 in *Mtb* [25].

In the crystal structure of DprE1 with TCA1 (PDB ID: 4KW5), two highly flexible loops (Loop I: residues 269–283; Loop II: residues 316–330) are totally disordered and unsolved [24]. The two regions are also invisible in the structures of DprE1 interacting with other benzothiazole inhibitors, as are most other DprE1 inhibitors [23,25]. The X-ray diffraction method is exceedingly difficult to solve the structures of such high flexible loops. Thus, when developing DprE1 inhibitors, the interactions derived from these two loops have never been considered [23,25–27]. However, these two flexible loops are never useless. Electron density analysis of all DprE1 crystal structures reveals that the two loops are located just above the substrate-binding pocket [23,26–29]. It is reasonable to deduce that these loops can be involved in interactions with bound inhibitors. In some cases, favorable interactions derived from Loop II have been detected [23,26,30]. In the DprE1-Ty36c complex (PDB ID: 4P8L), an extra H-bond (from Arg325) and two van der Waals interactions (from Leu317 and Asn324) are involved in Ty36c stabilization [30]. We propose that bridging or increasing the interactions between the two loops and DprE1 inhibitors might be an effective way to identify novel small molecules with improved inhibitory potency against both wild-type and drug-resistant mutants of DprE1.

In light of this hypothesis, we modeled the two missing loops in the DprE1-TCA1 structure through molecular dynamics (MD) simulations, and explored the potential functional sites within the two loops. Then, a series of small molecules were rationally designed by optimizing interactions with a newfound functional site. The experimental results verified LZDT1 as an excellent DprE1 inhibitor showing improved activity against drug-sensitive and drug-resistant *Mtb*. The sensitivity of LZDT1 against DprE1 Cys387-mutants was found to be higher than that of the template molecule TCA1 as well. Moreover, LZDT10 was designed as a new non-benzothiazole lead to fight against Cys387-mutants of DprE1. Directions for optimizing LZDT10 were revealed by the electrostatically driven structure-activity relationship (SAR) study at the same time. The present work explored the disordered loops in DprE1 and provided a functional site for designing new DprE1 inhibitors that can be potentially used to combat DR-TB. The same approach can be extended to exploit new functional sites in the missing regions of other targets, and further employ them for drug design and drug-resistance management.

## 2. Results and discussion

### 2.1. MD-based approaches to model the unsolved loops in the crystal structure of the DprE1-TCA1 complex

With reference to the crystal structure of the DprE1-Ty36c complex (PDB ID: 4P8L) [30], the two unsolved loop regions (Loop I: residues 269–283; Loop II: residues 316–330) in the DprE1-TCA1 structure (PDB ID: 4KW5) were modeled and supplemented, yielding an initial model for the complete DprE1-TCA1 complex (DprE1c-TCA1) (Fig. S1). The DprE1c-TCA1 model was then analyzed by 100 ns MD simulations. As shown in Fig. S2A, the DprE1c-TCA1 system achieved equilibrium at ~38 ns, and the root mean-square deviation (RMSD) of Cα was averaged as 1.98 Å. The ligand TCA1 reached equilibrium even earlier than the Cα, with RMSD (1.43 Å) also smaller than that of the Cα (Fig. S2B). The flexibility and local motion of the complete DprE1 in complex with TCA1 was reflected by the value of root mean-square fluctuation (RMSF). It is evident that the loop regions were much more flexible than the helix regions, especially for the regions of Loop I and Loop II (Fig. S2C). Such high flexibility may contribute to the difficult structure resolution of these two loop regions [24]. One point should be noted is that the regions around Leu317 were quite stable, even though the Loop II (residues 316–330) was overall flexible (Fig. S2C). Fluctuation of the DprE1 N-terminus exerted little effect on the binding sites of TCA1 due to its far distance to the substrate-binding domain.

Representative conformation of the DprE1c-TCA1 complex (Fig. 1) was produced based on cluster analysis of the trajectories collected during the 100 ns MD simulations (Table S2, Fig. S3). In the yielded MD representative conformation, it is noticeable that the two supplemented loops kept a stable conformation instead of being totally invisible. Further conformation superimposition revealed that the yielded MD representative conformation highly resembled the DprE1-TCA1 crystal structure (PDB ID: 4KW5), with a Cα RMSD of only 0.96 Å (Fig. S4). Furthermore, FAD, TCA1 and the residues (Lys418 and Ser228) forming H-bonds with TCA1 all exhibited no observed shifts (Fig. S4). For the atoms specifically involved in H-bond interactions, their distance shifts were limited within 1.0 Å (Fig. S4). These findings indicate that the results of MD simulations can capture the main atomic movements of the DprE1c-TCA1 complex. Current experimental ways (X-ray diffraction, NMR, and Cryo-EM) usually do not work well to solve structures of conformationally flexible loops, causing difficulties on exploring and exploiting the potential contacts between loop regions and ligands. Our work provides a successful case study concerning how to model the disordered loops using MD-based approaches.

### 2.2. Binding free energy decomposition and binding mode analysis reveal Leu317 as a new functional site directly interacting with TCA1

In the MD representative conformation of the DprE1c-TCA1 complex (Fig. 1), TCA1 was dominantly stabilized by residues including His132 (H132), Gly133 (G133), Lys134 (K134), Ser228 (S228), Tyr314 (Y314), Val365 (V365), Lys367 (K367), and Lys418 (K418). These residues were correspondingly the top contributors of favorable total free energy ($\Delta E_{pair}$) (Table S4, Fig. S5). For S228 and K418, they both provided favorable energy above −4.00 kcal/mol. Especially for K418, its total energy contribution even reached −11.82 kcal/mol (Table S4). The high energy contribution of these two residues can be explained by the H-bond networks formed in the DprE1c-TCA1 complex (Fig. 1). The NZ atom of K418 sidechain formed two H-bonds (2.8 Å and 2.9 Å) with N30 of TCA1 benzothiazole group and O12 of the TCA1 imide group, with MD occupancy being 66.20% and 34.63%, respectively (Fig. 1, Fig. S5, Table S5). Two H-bonds (2.7 Å and 3.6 Å) were also detected between the OG atom of the S228 sidechain and the O22 and O19 atoms of the TCA1 imide group (Fig. 1, Fig. S5, Table S5). Moreover, the occupancy sum of K418-derived H-bonds (100.83%) was higher than that of S228-derived H-bonds (91.64%) (Table S5). These characters were nearly identical to that of the DprE1-TCA1 crystal structure (PDB ID: 4KW5) [24]. This may explain why K418 contributed more favorable energy, or at least more electrostatic energy, than S228 (Table S4).

Although K134 and K367 formed no H-bond with TCA1, their electrostatic contributions (>−2.00 kcal/mol) were remarkable (Table S4). The van der Waals energy (>−1.00 kcal/mol) of these two residues cannot be neglected as well. All of these led to the high $\Delta E_{pair}$ contribution of K134 (-4.13 kcal/mol) and K367

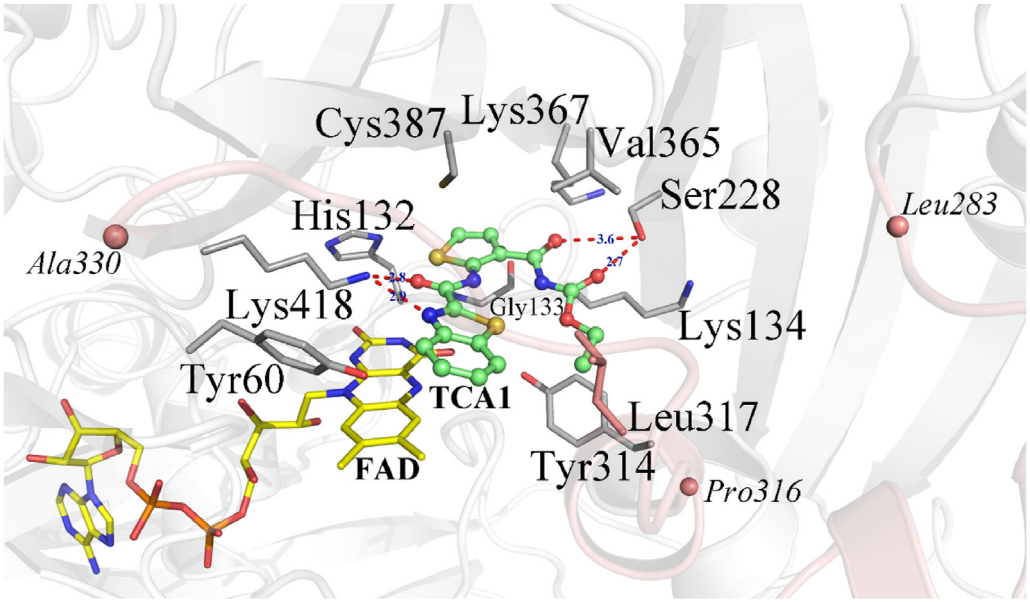


**Fig. 1.** Key interactions and H-bond patterns exhibited by TCA1 in the active site of the complete DprE1 structure. TCA1 is shown with the stick-and-sphere model. Color code: green, C; red, O; blue, N; gold, S. Important residues at the DprE1-TCA1 interface are shown in this stick model. Color code: grey, C; red, O; blue, N; gold, S. FAD is also shown in the stick model. Color code: yellow, C; red, O; blue, N; orange, P. The red dashed lines represent H-bonds. The two loops (residues 269–283, 316–330) are colored salmon, Leu317 is shown in the stick model.

(-2.54 kcal/mol) (Table S4). The van der Waals energy of V365 was above −2.00 kcal/mol due to its hydrophobic interaction with TCA1 benzothiazole and ethoxyl (Fig. S5, Table S4). It is noteworthy that the $\Delta E_{pair}$ contribution of C387 was beyond −2.00 kcal/mol as well, composed of −1.31 kcal/mol van der Waals energy, −0.66 kcal/mol electrostatic energy, and a rare favorable polar solvation energy (-0.042 kcal/mol) (Table S4). The $\Delta E_{pair}$ contributions of H132, G133 and Y314 all exceeded −1.50 kcal/mol. H132 and G133 formed interactions with TCA1 thiophene, and their energy contributions were dominantly derived from the van der Waals energy (about −1.00 kcal/mol) and electrostatic energy (about −0.60 kcal/mol) (Fig. S5, Table S4). For Y314, its phenyl ring interacted with TCA1 ethoxyl, resulting in the relatively larger van der Waals energy (-1.40 kcal/mol).

In most cases, the two loops (Loop I: residues 269–283; Loop II: residues 316–330) in DprE1 are too flexible to keep the right conformation, causing disorder and invisibility of the two loops in the crystal structures of DprE1 in complex with most inhibitors including TCA1 [23,24]. The whole of Loop II was only observed in quite limited cases (DprE1 with Ty36c, QN129, and CT319) [23,26,30]. Here with the two invisible loops being modeled and supplemented to the DprE1-TCA1 structure, the potential contacts of TCA1 with Loop I and Loop II were explored. It is found that the Loop I is evidently far from (over 10 Å) the binding site of TCA1, no interactions with TCA1 were detected in this region (Fig. 1). While in Loop II, the CG atom of the Leu317 (L317) sidechain was only about 5.0 Å away from the methyl of the TCA1 ethoxyl group (Fig. 1), and the hydrophobic interaction ($\Delta E_{VDW}$ = -0.65 kcal/mol) occurring between them was detected to be the main force in stabilizing the disordered Loop II (Fig. S5, Table S4). During the RMSF analysis of residues in the DprE1c-TCA1 system, the residue L317 showed high stability (Fig. S2C). The stability is a primary guarantee for a residue to be used for drug design. These characters together made L317 a newly discovered functional site located in the flexible Loop II. There also existed other hydrophobic residues (Trp230, Tyr314, Leu363, and Val365) around methyl of the TCA1 ethoxyl group. Among the four hydrophobic residues, Trp230 and Leu363 were far from the C38 atom (the C atom at the tail of TCA1 ethoxyl) of TCA1 (about 10 Å), Tyr314 and Val365 were two residues contributing significantly high free energy contribution (over −1.50 kcal/mol), it is not easy to optimize their interactions with TCA1 (Table S6). These residues were consequently not considered as potential functional sites for drug design. With TCA1 as the template molecule, new inhibitors with improved binding affinity toward both wild-type and TCA1-resistant mutants of DprE1 can be rationally designed by optimizing the interactions with the newfound functional site L317.

### 2.3. Rational design of benzothiazole derivatives with optimized hydrophobic interactions with Leu317

To optimize the hydrophobic interactions between L317 and TCA1, bioisosteric replacements of the methyl in TCA1 ethoxyl were performed with bioisosteric groups possessing a stronger hydrophobic field, yielding 14 novel TCA1 analogs ($1^{\#}$-$14^{\#}$) that scored above 0.95 (Table S7). TCA1 was re-established as such ($1^{\#}$) in the process. As shown (Table S7, Fig. S6), the eXtended Electron Distribution (XED) field point of the re-established TCA1 ($1^{\#}$) was of 98.6% similarity to that of the extracted TCA1 (from the MD representative conformation of the DprE1c-TCA1 complex), suggesting reliability of the computing methods adopted in the bioisosteric replacements. By comparing the XED field points of molecules $2^{\#}$-$14^{\#}$, we found that replacing the methyl of TCA1 ethoxyl with ethyl ($4^{\#}$), cyclopropyl ($6^{\#}$), 3-butynyl ($9^{\#}$), 3-butenyl ($10^{\#}$), and 2-mercaptoethyl ($13^{\#}$) all increased the hydrophobic field points between L317 and the replaced sites (Fig. S6). Further comparison between the integral hydrophobic field surfaces of TCA1, $4^{\#}$, $6^{\#}$, $9^{\#}$, $10^{\#}$ and $13^{\#}$ verified their improved hydrophobic interactions with L317, it is also determined that $6^{\#}$, $9^{\#}$ and $10^{\#}$ exhibited larger hydrophobic field surface enhancement than $13^{\#}$ and $4^{\#}$ (Fig. 2). To make sure that the hydrophobic interaction increased by the substituted groups in $4^{\#}$, $6^{\#}$, $9^{\#}$, $10^{\#}$ and $13^{\#}$ only occurred in the upper right of L317, the negative (red) and positive (blue) field points of these five molecules were compared to the

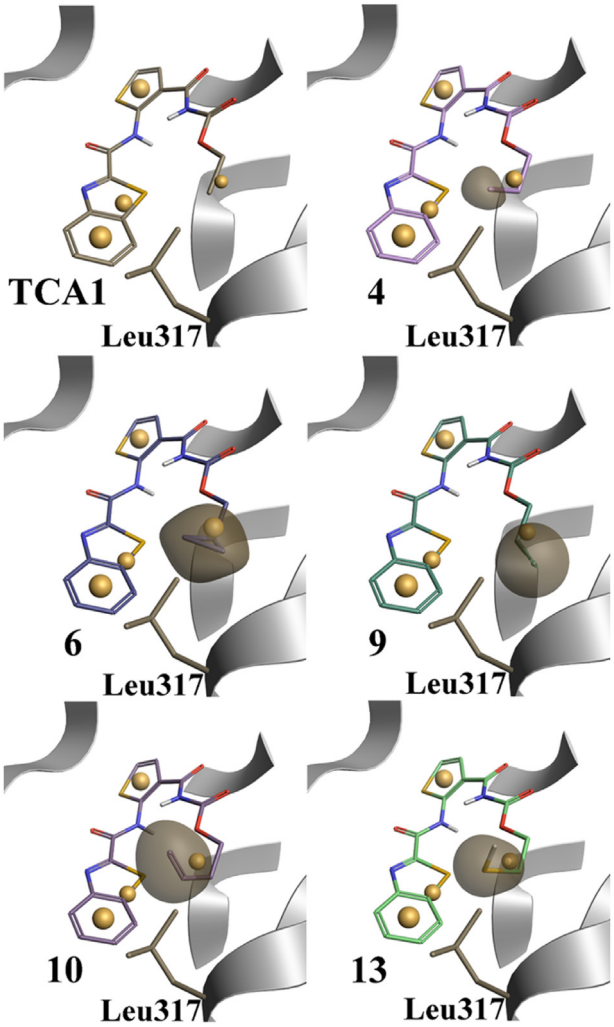


**Fig. 2.** The comparison of hydrophobic field surfaces derived from TCA1, $4^{\#}$, $6^{\#}$ (LZDT1), $9^{\#}$, $10^{\#}$, and $13^{\#}$. The integral hydrophobic field surfaces difference is shown in dark yellow. The hydrophobic fields of these molecules are shown as gold spheres. Each molecule is presented by the thin stick model. The active site of DprE1 is presented with the grey carton model. The residue Leu317 is shown as a stick model.

counterparts of TCA1 (Fig. S6). The field points of $4^{\#}$ were the closest to that of TCA1, but its hydrophobic field enhancement was fairly weak. The region underneath the $13^{\#}$ sulfydryl and in the upper right of L317 lacked a negative field point. Similarly, the region in the lower left of $9^{\#}$ alkynyl and the upper right of L317 also missed a negative field point. As for $6^{\#}$ and $10^{\#}$, their field points were both similar to that of TCA1. These defects made us give molecules $4^{\#}$, $9^{\#}$, and $13^{\#}$ up for further consideration. As a result, $6^{\#}$ and $10^{\#}$ were considered as two best molecules. Nevertheless, $6^{\#}$ was superior to $10^{\#}$ in the properties of field score, flexibility, and bioisosteric factor (BIF%) (Table S7). The hydrophobic force of $6^{\#}$ at the region nearby the upper right of the L317 sidechain was also stronger than that of $10^{\#}$ (Fig. S6). Thus, the molecule $6^{\#}$, named LZDT1 (Fig. 3A), was synthesized in priority for the following biological tests. The $^{1}$H NMR and MS spectra of TCA1 and LZDT1 were shown in Fig. S11~ Fig. S12.

### 2.4. Optimizing interactions with Leu317 potentiates bactericidal activity of LZDT1 against drug-resistant Mtb

As mentioned above, cyclopropyl is a perfect group to optimize the interactions between LZDT1 and L317. A subsequent biochemical and cellular assay showed that both the DprE1 inhibitory ($IC_{50}$: 50% inhibition concentration) and anti-mycobacterial activity (MIC: 99% minimum inhibitory concentration) of LZDT1 were significantly improved by the introduction of cyclopropyl. Compared to TCA1, LZDT1 was over four times more potent in inhibiting DprE1 ($IC_{50}$) and at least two times more efficacious in *Mycobacterium* strains (MIC) (Table 1, Fig. 3B and C). To determine the bactericidality of LZDT1 relative to TCA1 and rifampin (RIF), a 21-d killing assay experiment was performed. The three drugs (20 × MIC for each drug) were obviously active against *M. bovis* bacillus Calmette-Guérin (BCG) and *Mtb* H37Rv, reducing cfu (colony-forming unit) by about 3 logs in 21 d. Remarkably, treatment with LZDT1 resulted in a greater cfu reduction relative to TCA1 and RIF over the first 7 d (Fig. 3Da & Dc). The DprE1-targeting of LZDT1 and TCA1 was verified by the cfu and MIC shifts in DprE1-overexpressing BCG (Fig. 3C, Fig. 3Db). Relative to TCA1, LZDT1 caused a smaller cfu reduction in BCG with DprE1 overexpressed, indicating the improved target-specificity of LZDT1.

The activity of LZDT1 on DR-TB was emphatically evaluated. Relative to TCA1, LZDT1 was found to be of higher activity against a clinically isolated RIF-resistant *Mtb* H37Rv, with MIC value about half that of TCA1 (Fig. 3C). Even though both TCA1 and LZDT1 reduced cfu by about 3.5 logs after a 21-d treatment, a faster cfu reduction of the RIF-resistant strain was observed in the LZDT1-treated group (Fig. 3Dd). The improved activity of LZDT1 was also observed in fighting against multidrug-resistant *Mtb*. As revealed by the MIC values listed in Table 2, LZDT1 was at least two times more potent than TCA1 when encountering the HD1~HD5 strains which were resistant to more than one frontline anti-TB drugs including RIF and INH. As a newly released anti-TB drug targeting ATP synthase, BDQ is a preferred choice for MDR-TB treatment [31–33]. In our tests, sensitivity of HD1~HD5 to LZDT1 or BDQ was variable (Table 2), suggesting the existence of resistance to the two compounds in clinical strains of MDR-TB. However, it should be noted that no significant cross resistance was observed between LZDT1 and BDQ. Our results indicate that LZDT1 has real potential as a new tool in the treatment of DR-TB or even MDR-TB.

In the field of drug optimization, cyclopropyl is frequently used as a hydrophobic group to improve drug bactericidality [34–36]. For example, SAR exploration of pyrazolopridones, a class of DprE1 inhibitors, revealed that introducing cyclopropyl could result in the improvement of *Mtb* MIC [37]. The success of cyclopropyl in improving drug potency drives us to replace the cyclopropylmethyl in LZDT1 with other carbocyclic groups containing four or more carbons in the cycle, yielding LZDT2 (cyclobutylmethyl substitution), LZDT3 (cyclopentylmethyl substitution), LZDT4 (cyclohexylmethyl substitution) and LZDT5 (cyclobutyl substitution) (Fig. 4A, Figs. S13–S16). Nevertheless, all alterations to the LZDT1 cyclopropylmethyl showed a dramatic loss in DprE1 inhibitory and anti-mycobacterial activity (Table 1). Among LZDT2~LZDT5, only LZDT2 kept acceptable potency to DprE1 and drug-sensitive *Mtb* H37Rv, with $IC_{50}$ and MIC reaching 0.098 ± 0.019 μM and 3.01 μM, respectively (Table 1). However, one point should be noted is that, similar to LZDT1, the LZDT1-derived LZDT2 is provided with better activity than TCA1 in fighting against MDR-TB as well (Table 2).

Considering the fact that *Mycobacterium* strains were intracellular pathogens, we further investigated the intracellular anti-mycobacterial activity of LZDT1 and LZDT2 using a macrophage infection model. It is known that LZDT1 and LZDT2 are not as potent as RIF in inhibiting *Mtb* H37Rv (Fig. 3C). However, the log10 cfu reduction in macrophages caused by LZDT1 (1.1) and LZDT2 (0.9) was found to be similar to that of RIF (1.1) and larger than that of TCA1 (0.6) under the same condition (Table S8), indicating higher bacterial and cell permeability of LZDT1 and LZDT2. Moreover,

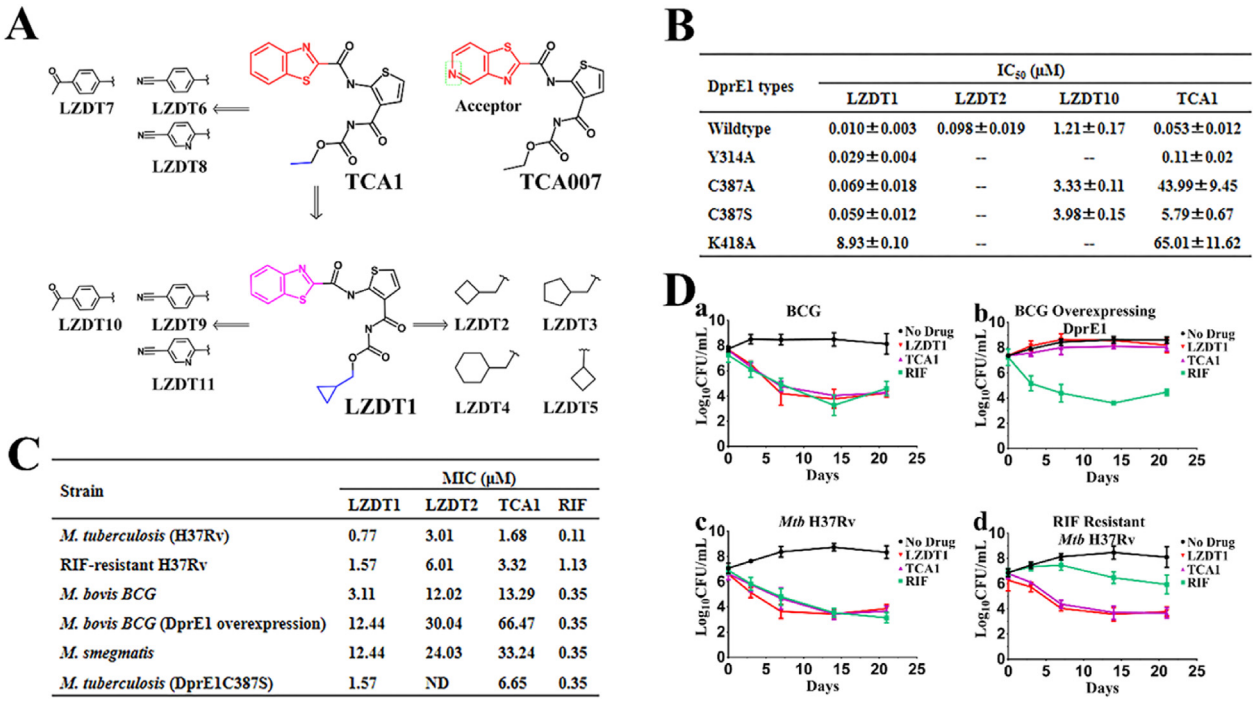


**Fig. 3.** Rational design and bioactivity evaluation of benzothiazole analogs. (A) Structure-guided optimization strategy for benzothiazole analogs. (B) $IC_{50}$ against wildtype and mutant DprE1. Y314A, C387A and K418A are DprE1 proteins with Tyr314, Cys387 and Lys418 being replaced by Ala, respectively. C387S is DprE1 protein with Cys387 being replaced by Ser. (C) MIC against *Mycobacterium* strains. *M. bovis BCG* (DprE1 overexpression) is the *M. bovis BCG* strain overexpressing DprE1. *M. tuberculosis* (DprE1C387S) is the *M. tuberculosis* strain harboring DprE1 with C387 replaced by Ser. (D) In vitro kinetic killing assay of each compound using 20 × MIC in 7H9 medium. $IC_{50}$ means 50% inhibition concentration, MIC means 99% minimum inhibitory concentration.

LZDT1 and LZDT2 showed optimized cytotoxicity. It is shown that, relative to that of TCA1, the $IC_{50}$ of LZDT1 against HepG2, SH-SY5Y, and HEK-293 cell lines was reduced by 1/2−1/3 (Table S9). The optimized cytotoxicity is of significance for anti-TB drugs, especially when considering the lengthy regimen of TB treatment [3].

Among current small molecules showing inhibitory activity towards DprE1, none had been designed by optimizing interactions with residues in the conformationally flexible Loop I and Loop II [19]. It is clear that, due to the optimized interaction with L317, LZDT1 was provided with improvement in target inhibition, target specificity, cytotoxicity, and bactericidal activity against drug-sensitive/-resistant *Mycobacterium* strains. Moreover, LZDT1 and its analogue LZDT2 were both superior to TCA1 in inhibiting MDR-TB. These optimized characters together with high permeability and low cytotoxicity indicated promising druggability of LZDT1 and LZDT2. Our attempts to bridge the hydrophobic interaction between Loop II and TCA1 using cyclopropyl not only gained a prominent inhibitor (LZDT1) for DprE1, but also validated L317 as a new functional site to be exploited for drug potency improvement and drug-resistance management.

### 2.5. Optimizing interactions with Leu317 sensitizes LZDT1 to Cys387-mutants of DprE1

Covalent inhibitors like benzothiazinones (BTZs) are known to form a covalent adduct with C387 and their potency in inhibiting DprE1 is C387-dependent [26,38,39]. As a result, the covalent inhibitors for DprE1 are commonly inactive against C387-mutants of DprE1 [40]. The C387-mutation is actually the most common mechanism for DprE1-mediated drug resistance of *Mycobacterium*. Hitherto, five spontaneous DprE1 mutants at C387 have been reported (C387S, C387G, C387A, C387 N, and C387T), yielding drug-resistant *Mycobacterium* strains [19,40]. For example, the C387G and C387S variants of DprE1 could increase the MIC of BTZs by at least 1000-fold [40,41]. For benzothiazole derivatives, they behave as competitive noncovalent inhibitors for DprE1 and are unable to bind covalently to C387 [24,25]. But C387 is never an invalid site for benzothiazoles. In the DprE1c-TCA1 structure, evident sulfur-sulfur (S-S) interactions were detected between the SG atom of C387 and the two S atoms of TCA1 (thiophene S15 and benzothiazole S27). Such interactions were considered to increase TCA1 binding by maintaining preferred orientations of these S-containing rings [42]. Indeed, C387 was predicted as a hot-spot in the DprE1-TCA1 interaction by computational alanine scanning (Table S11). The greatly decreased sensitivity of TCA1 to DprE1 mutants at C387 (C387A/387S) verifies the C387-dependence of TCA1 (Fig. 3B). Thus, we speculated that the bactericidality of TCA1 would decrease when encountering *Mycobacterium* strains containing C387-mutants of DprE1. As expected (Fig. 3C), the C387S mutation in DprE1 caused a 4-fold increase in the MIC of TCA1 against *Mtb* H37Rv (1.68 μM vs 6.65 μM).

The foregoing results lead us to suggest that reducing C387-dependence of DprE1 inhibitors will likely decrease the emerging resistance caused by C387-mutation in DprE1. For this very purpose, optimizing interactions at other sites of the DprE1-TCA1 system is worth exploring to produce new benzothiazole derivatives sensitive to C387-mutants of DprE1. Just as in the design of LZDT1, the improved hydrophobic interactions with L317 would compensate for the ligand binding affinity loss caused by C387 mutation in DprE1, leading to the reduced C387-dependence of LZDT1 in inhibiting DprE1. As expected, the $IC_{50}$ of LZDT1 only exhibited slight shifts in inhibiting DprE1 and its variants (DprE1C387A, DprE1C387S) (Fig. 3B). The MIC of LZDT1 against the H37Rv-DprE1C387S strain (*Mtb* H37Rv strain harboring C387S mutation of DprE1) displayed a much lower increase as well, from 0.77 μM to 1.57 μM (Fig. 3C). Moreover, the decreased C387-

**Table 1**
DprE1 Inhibitory activity ($IC_{50}$) and MIC against *Mtb* H37Rv for TCA1 and analogs.

| Index | Structure | MIC (μM) | $IC_{50}$ (μM) | Index | Structure | MIC (μM) | $IC_{50}$ (μM) |
|---|---|---|---|---|---|---|---|
| TCA1 | 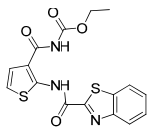 | 1.68 | 0.053 ± 0.012 | LZDT6 | 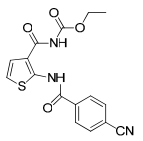 | >300 | >64 |
| LZDT1 | 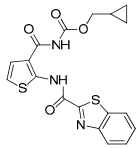 | 0.77 | 0.010 ± 0.003 | LZDT7 | 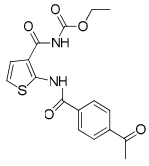 | >300 | 36.43 ± 4.71 |
| LZDT2 | 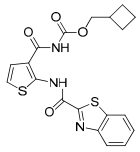 | 3.01 | 0.098 ± 0.019 | LZDT8 | 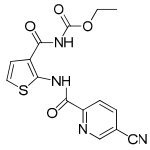 | >300 | 41.24 ± 6.52 |
| LZDT3 | 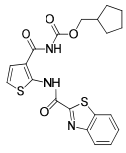 | >250 | 22.38 ± 2.87 | LZDT9 | 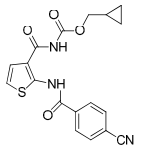 | >250 | 18.87 ± 2.74 |
| LZDT4 | 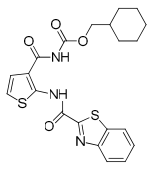 | >250 | >64 | LZDT10 | 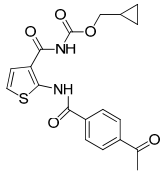 | 51.76 | 1.21 ± 0.17 |
| LZDT5 | 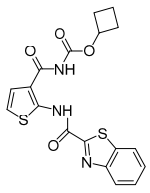 | >250 | 18.57 ± 2.16 | LZDT11 | 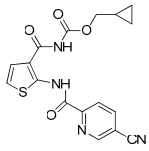 | 215.58 | 11.54 ± 1.62 |

**Table 2**
MIC values for selected benzothiazole derivatives and anti-TB drugs against five isolated clinical strains of MDR-TB.

| Clinical isolates of MDR-TB | MIC (μM) | | | | | |
|---|---|---|---|---|---|---|
| | LZDT1 | LZDT2 | TCA1 | BDQ | RIF | INH |
| HD1 | 1.94 | 1.88 | 4.15 | 0.07 | 1.90 | 18.23 |
| HD2 | 3.88 | 3.76 | 8.33 | 0.29 | 3.82 | 36.45 |
| HD3 | 0.97 | 1.88 | 2.07 | 0.14 | 0.95 | 9.11 |
| HD4 | 1.94 | 3.76 | 8.33 | 0.58 | 1.90 | 18.23 |
| HD5 | 1.94 | 3.76 | 8.33 | 0.07 | 3.82 | 36.45 |

dependence of LZDT1 would probably reduce the mutation risk of C387 in DprE1. For these reasons, optimizing interactions with L317 can be taken as a feasible way to manage the drug-resistance mediated by C387-mutation of DprE1. The success of LZDT1 verifies the assertion that the potential contacts with disordered loop regions in DprE1 (Loop I and Loop II) is worth exploiting to improve the affinity of new inhibitors for DprE1 as well as to fight against drug-resistant mutants of DprE1.

### *2.6. Optimizing interactions with Leu317 produces a nonbenzothiazole lead with reduced Cys387-dependence*

Knowing that C387-mutation is a common mechanism for DprE1-mediated resistance, and S-S interaction acts to strengthen C387-dependence of benzothiazole inhibitors, removing the S-containing groups in benzothiazole inhibitors would likely be

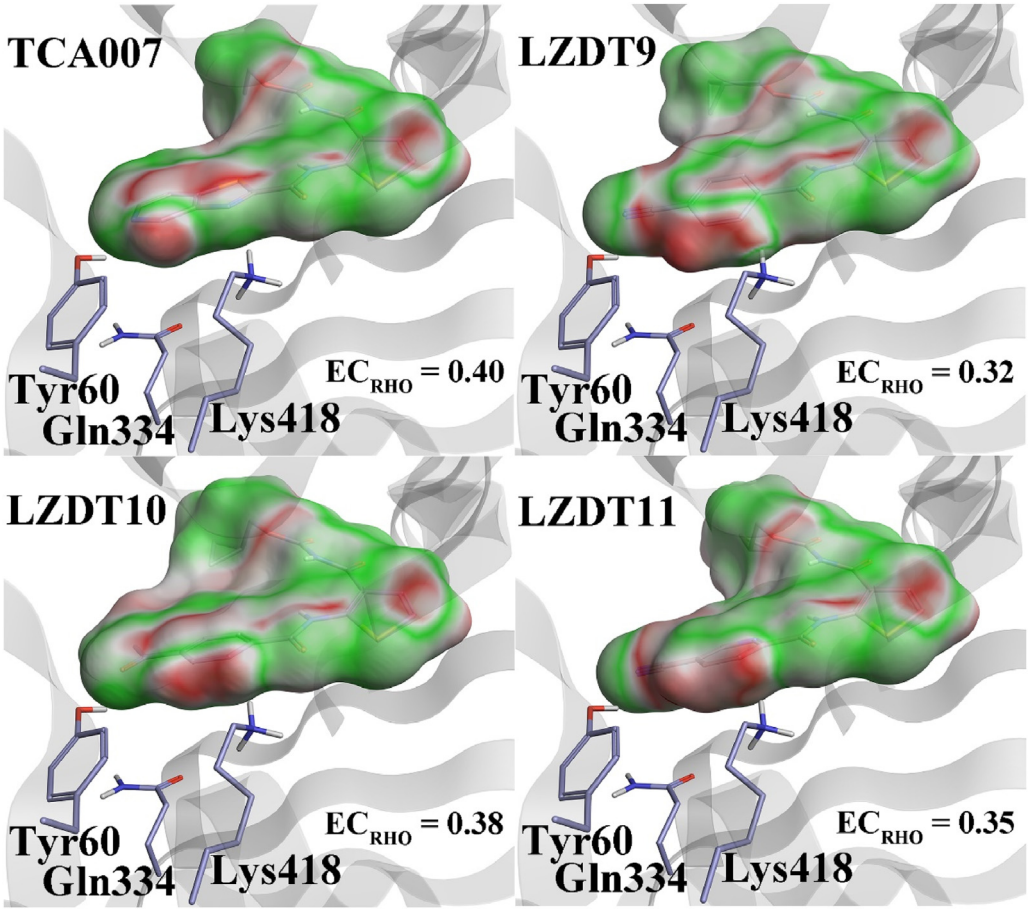


**Fig. 4.** Comparison of the electrostatic complementarity (EC) matches and $EC_{RHO}$ scores of TCA007 and LZDT9~LZDT11. The electrostatic complementary and clashing regions are colored in green and red, respectively. The four molecules, Tyr60, Gln334 and Lys418 are shown with thin stick model. The active site of DprE1 is shown as a light grey carton model.

another way to combat C387-mutants of DprE1. Based on the design of TCA007 ($IC_{50}$ = 0.0053 ± 0.18 μM; MIC = 0.089 ± 0.0066 μM) reported by Liu et al. [25], three S-free groups (benzonitrile, acetophenone, and nicotinonitrile) with similar XED field to TCA007 pyridothiazole were used to replace the benzothiazole group in TCA1, yielding three small molecules LZDT6~LZDT8 (Table S10, Fig. 3A, Figs. S17–S19). Compared to the benzothiazole group in TCA1, its substituents (pyridothiazole group, benzonitrile group, acetophenone group, nicotinonitrile group) in TCA007 and LZDT6~LZDT8 all formed an extra H-bond with the hydroxyl of the Tyr60 (Y60) sidechain (Fig. S8). However, our attempts to replace the TCA1 benzothiazole group with the S-free groups failed to improve the DprE1-inhibitory activity and bactericidality ($IC_{50}$ > 30 μM, MIC>300 μM) (Table 1, Fig. S10). Inspired by LZDT1, the methyl in the ethoxyl group of LZDT6~LZDT8 was replaced by cyclopropyl to optimize the interactions with L317. As expected, the resultant LZDT9~LZDT11 (Figs. S20–S22) were provided with improved potency against DprE1 and *Mtb* H37Rv (Table 1, Fig. S10). Especially for LZDT10, its $IC_{50}$ and MIC were improved to 1.21 ± 0.17 μM and 51.76 μM, respectively (Table 1). It is evident that the optimized interaction with L317 improves the bioactivity of LZDT10 to an acceptable level. To our knowledge, the acetophenone group in LZDT10 is new to current DprE1 inhibitors. Moreover, as a group containing no S atom, the acetophenone would not form S-S interaction with the SG atom of C387, leading to the decreased C387-dependence of LZDT10 in inhibiting DprE1 (Fig. 3B). With the optimized interaction with L317, the acetophenone-containing LZDT10 is competent to be a nonbenzothiazole lead to fight against mycobacterial resistance caused by C387-mutation in DprE1.

Electrostatic complementarity (EC) of protein-ligand complexes is a useful tool to predict electrostatically driven ligand binding affinity changes [43]. Thus, to better understand the basis of activity reduction, the EC match of DprE1 in complex with TCA007 and LZDT9~LZDT11 was assessed. Cyclopropyl is a specific group to increase the hydrophobic field, its presence exerted little influence on local EC (Fig. 4). The most significant EC changes were detected in the regions around the TCA007 pyridothiazole and its bioisosteric groups. Compared with TCA007 pyridothiazole groups, the EC match of acetophenone group in LZDT10, nicotinonitrile group in LZDT11, and benzonitrile group in LZDT9 decreased in order (Fig. 4), perfectly matching the sorting order of overall EC scores ($EC_{RHO}$) and bioactivity ($IC_{50}$ and MIC) of TCA007 and LZDT9~LZDT11 (Table 1, Fig. 4) [25]. The results of an electrostatically driven SAR study revealed that the EC matching degree of groups used to replace TCA007 pyridothiazole was directly related to the bioactivity of the resultant small molecules.

In the DprE1-TCA007 structure, three residues, Tyr60 (Y60), Gln334 (Q334), and K418, were involved in electrostatic interactions with the pyridothiazole group in TCA007. The N atom of the pyridine ring and the thiazole ring showed fairly good EC with the side-chains of Y60 and K418, respectively. Whereas at the interface of the pyridine ring and the amide side-chain of Q334, an evident electrostatic clash was visualized (Fig. 4). Attempts to minimize such electrostatic clash would be worth a shot towards improving the bioactivity of TCA007. Compared to TCA007

pyridothiazole, the three bioisosteric groups (benzonitrile, acetophenone, and nicotinonitrile) in LZDT9~LZDT11 all showed an inferior EC match with K418 and Q334 (Fig. 4). Only LZDT10 acetophenone matched better with Tyr60 (Y60), resulting in the best MIC (51.76 μM) and $IC_{50}$ (1.21 ± 0.17 μM) (Table 1). However, the only advantage of LZDT10 over TCA007 was far from enough to offset the negative effects caused by the decreased EC with the other two residues (Q334 and K418). Thus, the EC matching degree with Q334 and K418 is a key cause of the activity gap between TCA007 and the novel lead compound LZDT10. At this point, optimizing the EC of acetophenone to Q334 and K418 (e.g. making optimizations on the phenyl of acetophenone) would be a practical way to design novel acetophenone derivatives with higher activity against DprE1 and *Mycobacterium* strains, leading to the development of a class of anti-mycobacterial agents.

## 3. Conclusion

In summary, we provided a feasible way to exploit the potential functional sites in missing loops of a drug-target complex. MD-based approaches were initially adopted to supplement the two missing loops (Loop I and Loop II) in the DprE1-TCA1 structure. Then in the complete DprE1-TCA1 structure, L317 in the Loop II was discovered as a new functional site to improve the activity of DprE1 inhibitors and to combat mycobacterial resistance. As expected, the resultant LZDT1 was superior in inhibiting DprE1 and combatting drug-sensitive/-resistant *Mycobacterium* strains. Moreover, relative to TCA1, the improved activity of LZDT1 and its analogue LZDT2 were highlighted. Optimizing interactions with L317 was verified as a practical way to overcome the drug-resistance mediated by C387 mutation in DprE1. An added benefit of this work is that the acetophenone-containing LZDT10 is a novel anti-mycobacterial lead targeting DprE1. Through electrostatically driven SAR study, improving the EC matching degree of acetophenone with Q334 and K418 was pointed as a direction for LZDT10 optimization. Our work highlights the power of functional sites in disordered loops to design new DprE1 inhibitors with potent activity against DR-TB. More widely, the DprE1-TCA1 system is not the only target-drug complex possessing conformationally flexible loops. Given the technical difficulties in solving structures of such loops, we can envision that our approaches to exploit and to optimize potential contacts with disordered loops in targets will inspire new directions for drug development against TB and beyond.

## 4. Experimental section

### 4.1. Structure construction of the complete DprE1-TCA1 complex

Two disordered loop regions (residues 269–283, 316–330) were not resolved in the crystal structure of DprE1-TCA1 (PDB ID: 4KW5) [24]. While in the crystal structure of the DprE1-Ty36c complex (PDB ID: 4P8L), the same two disordered loop regions are contained [30]. So these missed regions in the 4KW5 was filled up by using 4P8L as a reference structure. Initially, the atomic coordinates of 4KW5 were superimposed on 4P8L in the PyMOL 1.3r1 edu software [44]. Then, the DprE1 structure from the reference structure plus the TCA1 structure superimposed on the reference structure were extracted integrally to obtain the complete DprE1-TCA1 (DprE1c-TCA1) complex. This was further used as the initiating structure for prospective molecular dynamics (MD) simulations.

### 4.2. Molecular dynamics simulations of the DprE1c-TCA1 complex

MD simulations for the DprE1c-TCA1 complex were carried out by the AMBER12 package [45]. To prepare for MD simulations, the DprE1c-TCA1 complex was solvated in a rectangular box of TIP3P (transferable intermolecular potential with three points) water, and the minimum solute wall distance was set as 12 Å [46]. Parameters and charges of TCA1 were set by the GAFF (General Amber Force Field) and the AM1-BCC (semiempirical with bond charge correction) method, DprE1 parameters were depicted by the bioorganic systems force field (ff99SB) [47–49]. Global charge of the DprE1c-TCA1 system was neutralized by adding counterious. The energy of the DprE1c-TCA1 complex was minimized by the successive application of the steepest descent method (5000 steps) and the conjugated gradient method (5000 steps) [50]. After all of these preparations, the DprE1c-TCA1 system was equilibrated as follows: heating from 0 to 300 K in the NVT ensemble (canonical ensemble) in 500 ps, density equilibration with weak restraints for 500 ps, and unrestrained equilibration in constant pressure at 300 K for 5 ns. Thereafter, the production phase of MD simulations was conducted by running for 100 ns in the same conditions as that of the equilibration phase [51]. Particularly for the production phase, three individual 100 ns MD simulations at different seeds were performed without any restraints. Noticeably, both equilibration and production phases were performed in the isothermal isobaric (NPT) ensemble using a Berendsen barostat [52].

Results of the three MD replicates were subjected to Ambertools13 package for further analysis. Data from the three replicates were averaged, and the average-linkage algorithm was utilized to cluster the MD simulations based on the trajectories generated in the MD process. All the detail of MD simulations was similar to our former reports [51,53–56].

### 4.3. Binding free energy calculation and pairwise per-residue free energy decomposition

The molecular mechanics-Poisson-Boltzmann surface area (MM-PBSA) method in Amber12 software was adopted to calculate binding free energy ($\Delta G_{bind\text{-}cal}$) of the DprE1c-TCA1 complex [57]. The entropy contributions ($T\Delta S$) of the DprE1c-TCA1 system was calculated by using normal-mode analysis in the nmode module of AMBER 12 [58]. In the present research, the absolute binding free energy ($\Delta G_{bind\text{-}abs}$) of the same complex was further estimated by considering the entropy contributions ($T\Delta S$) [51]. The detail process was conducted based on our previous researches [51,53].

Defining the interaction energy spectra helps to elaborate the interactions between DprE1 and TCA1 [59,60]. Here, pairwise per-residue free energy decomposition was performed to scheme the energy spectra of the DprE1c-TCA1 complex using the MM-PBSA method in the mmpbsa.py module of AmberTools13 [61–64]. The energy decomposition process was conducted similar to our former reports [51,59].

### 4.4. Computational alanine scanning and site-directed mutagenesis

To predict potential residues essential for the binding of TCA1 to DprE1, computational alanine scanning (CAS) of the DprE1c-TCA1 complex was performed [65]. Here in the research, residues contributing above −1.50 kcal/mol binding free energy were subjected to CAS. The calculated binding free energy changes ($\Delta\Delta G_{bind\text{-}cal}$) caused by mutations were calculated by the MM-PBSA method. The detail process was similar to our former reports [51,54,66].

The hot-spots predicted by CAS were further individually mutated into Ala by site-directed mutagenesis. Here in the present research, fast mutagenesis kit (Vazyme, China) was adopted to mutate the *DprE1* gene according to the protocol. Primers used in the site-directed mutagenesis were designed accordingly and listed in Table S1.

### 4.5. Construction of the fragment library for bioisosteric replacements

The fragments of commercial drugs or pesticides fragments possessing link points from PADFrag database, and the structure data of commercial fragments on the official websites of ChemDiv and Enamine were downloaded [67–70]. We used the eXtended Electron Distribution (XED) molecular mechanics force field in the Spark software (Cresset) to generate the 3D active conformations of these downloaded fragments [71]. The fragment library used for bioisosteric replacements was composed of these active conformations (removing the repeated structures).

### 4.6. Expression and purification of Mtb DprE1 and the mutants

The wildtype and mutant *Mtb* DprE1 proteins were expressed as former reports with some modifications [25,30]. The *wildtype DprE1* (*DprE1WT*) gene was incorporated into the pCold II vector (TaKaRa, Japan), and the two molecular chaperones (GroES and CPN60.2) from *Mtb* were subcloned into the two multi-cloning sites of pCDF-Duet1 vector. The two generated vectors were co-transformed into the competent *E. coli* BL21 (DE3) cells. The *E. coli* strain was cultured in LB medium (adding appropriate ampicillin and streptomycin) at 37 °C for ~6 h and subsequently induced with 0.8 mM IPTG at 15 °C for 20 h. Cultures were collected by centrifugation and re-suspended in a 25 mL equilibration solution of $Ni^{2+}$-NTA resin (Qiagen, Germany) containing 0.5 mM EDTA-free PMSF. After incubating with 1 mg/mL lysozyme on ice for 1 h, the re-suspended cultures were disrupted by sonication for 8 min (10 s work/10 s stop) and centrifuged at 12000 *g* for 30 min at 4 °C. The obtained supernatant was loaded onto a $Ni^{2+}$-NTA column (Qiagen, Germany) and eluted with gradient elution buffer ($Ni^{2+}$-NTA equilibration solution plus 250/500 mM imidazole). The purified recombinant DprE1WT protein was digested by Enterokinase (Solarbio, China) to remove the expression tag in the recombinant DprE1WT protein, after being dialyzed against 10 mM PBS (pH 7.4) overnight. The digested DprE1WT protein was further purified by a $Ni^{2+}$-NTA column (Qiagen, Germany) as mentioned above. The mutant DprE1 (DprE1MT) proteins were expressed and purified similarly.

### 4.7. DprE1 inhibition assay

DprE1 assays were performed at 30 °C in 384-well black plates (catalog no. 3573, Corning) in a final volume of 30 μL. Briefly, DprE1 (300 nM), FAD (1 μM), HRP (0.2 μM), and Amplex Red (50 μM) in 50 mM glycylglycine (pH 8.0) containing 200 mM potassium glutamate and 0.002% Brij-35 were incubated with different concentrations (0–64 μM) of test compounds at 30 °C. 10 min later, 300 μM farnesyl-phosphoryl-β-D-ribofuranose (FPR) was added to the incubated reaction mixture. The increase in fluorescence intensity (λex/λem: 530/595 nm), related to the conversion of Amplex Red to resorufin, was monitored on a microplate reader (TECAN Infinite M200) in kinetic mode at 30 °C. In the wells for negative controls, inhibitors were replaced by equivalent DMSO. TCA1 was used as a positive control, and the background fluorescence (test wells without adding FPR) was subtracted. All inhibitors were dissolved in DMSO, and the final concentration of DMSO was fixed at 1% (v/v). The $IC_{50}$ values were obtained by plotting the initial velocities with inhibitor concentration. The inhibitory effects of TCA1 and its analogs on DprE1MT proteins were explored similarly.

### 4.8. Bacterial strains, culture conditions, and chemicals

*Mycobacterium tuberculosis* H37Rv (*Mtb* H37Rv), *M. bovis Bacille Calmette–Guerin* (Pasteur 1173P2), *M. smegmatis* mc2155, and drug resistant *M. tuberculosis* strains were grown at 37 °C in Middlebrook 7H9 broth (Difco) supplemented with 0.2% glycerol, 0.05% Tween 80, and 10% albumin-dextrose-catalase (ADC) or on Middlebrook 7H10 agar (Difco) supplemented with 0.2% glycerol and 10% oleic acid-albumin-dextrose-catalase (OADC). All chemicals were purchased from Sigma-Aldrich unless otherwise stated.

### 4.9. Minimal inhibitory concentrations (MICs) measurement

Microplate alamar blue assay was employed to determine the MICs (99% minimum inhibitory concentration). Four *Mycobacterium* strains used in MICs assay were *M. bovis Bacille Calmette–Guerin* (BCG), BCG overexpressing DprE1, *Mtb* H37Rv, and rifampin (RIF) resistant *Mtb* H37Rv. Each strain was precultured at 37 °C in Middlebrook 7H9 broth (Difco), then diluted with 7H9 broth to yield a broth of ~$10^6$ CFU/mL. Thereafter, 100 μL the diluted broth plus 0–80 μg/mL test compounds was added to wells of the 96-well plates. The plates were then covered by a sticky film to prevent evaporation and incubated at 37 °C for 7 days. To determine MIC values, the reaction mixture was kept at 37 °C for another 24 h after adding 10 μL alamar blue (0.025% w/v) and Tween 80 (0.05% v/v) to each test well. The inhibitory effect was determined by measuring fluorescence using an envision 2103 multilabel reader (Perkin-Elmer Life Sciences, USA) with excitation at 530 nm and emission at 590 nm. In the MICs measurement, all compounds were prepared at 100 × stocks in DMSO, serial dilutions of the compounds were prepared in the same solvent which was fixed at 1% (v/v). The organic solvent DMSO was taken as negative control, while TCA1 and RIF were used as positive controls. The MIC here was defined as the minimum concentration of the compound that caused a 99% reduction of absorbance relative to that with the negative controls.

The same method mentioned above was also employed to test the potency of newly designed compounds against DR-TB. Herein, five clinically isolated MDR-TB (multi-drug resistant TB) strains (HD1~HD5) reported by Wu et al. (2020) were selected as test strains [10]. TCA1 and three anti-TB drugs including RIF, Isoniazid (INH) and Bedaquiline (BDQ) were used as positive controls.

### 4.10. Conditional knockout of DprE1 and C387S mutant construction

The *DprE1* gene (Rv3790) together with a flanking DNA sequence (about 2 kb) was amplified from *M. smegmatis* $mc^2155$ using primers A (5′- GATCAAGCTTACGCCCTCGATCGTCCTG-3′) and B (5′- TGCAGCGGCCGCCAGCGCGTGCAGCGAG -3′), and cloned into the pUC18 vector. A 1.9 kb kanamycin resistance cassette carrying the *aphA3* gene was inserted within the *DprE1* gene. The 3.9 kb (2 kb + 1.9 kb) fragment containing *Rv3790::aphA3* was transferred to create the final recombination HD DprE1 plasmid which was subsequently introduced into *M. smegmatis* $mc^2155$ by electroporation for selecting single crossover HD1. For conditional knockout, a rescue plasmid containing the *DprE1* gene was cloned into the temperature-sensitive plasmid pCG76 and was introduced into HD1 by electroporation. Transformants were selected on LB agar plates at 30 °C. Potential conditional knockout clones were confirmed by Rv3790-specific probe.

The *DprE1* gene was amplified together with Rv3789 by using primers Rv3790 forward and Rv3790 reverse and cloned into the pCR-Blunt II-TOPO vector (Invitrogen). The replacement of Cys387 by Ser (DprE1C387S) was carried out using the Stratagene

QuikChange II site-directed mutagenesis kit (Agilent Technologies, USA) with specifically designed primers. The mutant fragments were ligated into the pND255 vector with a hygromycin resistance cassette. The integrative vector was then transformed and integrated at the L5-attB site of *M. smegmatis* $mc^2155$ and *M. tuberculosis* H37Rv. Transformants were selected on 7H10 agar plates. A specific primer was used to repeat the site-directed mutagenesis to obtain the DprE1C387S mutant.

### 4.11. Antimicrobial activity against Mycobacterium strains

The *Mycobacterium* strains at logarithmic phase were diluted to $OD_{600}$ = 0.1 by fresh 7H9 medium plus 20 × MIC LZDT1, and cultured under the conditions of 37 °C and 80 rpm. The cultures were sampled at different times (day 0, 3, 7, 14, and 21) followed by being spread on the solid 7H10-ADC media evenly. CFU of the *Mtb* H37Rv strain was then visually counted after incubation at 37 °C for 4 weeks. In the testing process, 20 × MIC RIF and TCA1 were taken as positive controls, and DMSO (1%, v/v) was taken as a negative control. Under all assay conditions, the final concentration of DMSO was fixed at 1% (v/v).

### 4.12. Intracellular anti-mycobacterial activity

The mouse macrophages cell line J774A.1 was purchased from National Infrastructure of Cell Line Resource (Beijing, China) and cultured in Dulbecco's modified eagle medium (DMEM) supplemented with 10% fetal bovine serum (FBS). The cells were grown in a humidified incubator (37 °C, 5% $CO_2$). For infection, cells were seeded in a 24-well plate containing 2 × $10^5$ cells/mL in antibiotic free media and incubated for 24 h at 37 °C. The *Mtb* H37Rv strain was grown at 37 °C to mid-log phase in 7H9 medium supplemented with 10% OADC, and 0.05% Tween 80. The cultured *Mtb* H37Rv was filtered with 80 μm filter membrane and adjusted to $OD_{600}$ = 0.1. The J774A.1 cells were infected at a MOI of 10:1, incubated for 4 h and washed with 10 mM sterile PBS (pH 7.4) for three times to remove non-internalized bacteria. The infected cells were cultured further in 1 mL DMEM medium containing 10% FBS for three days at 37 °C in the presence or absence of 5 μg/mL tested benzothiazole derivatives, with 5 μg/mL RIF being the positive control. After three days incubation, cells were lysed in 200 μL cell lysis buffer for 5 min. The number of viable bacteria in each well was numerated by plating on Middlebrook 7H11 agar plates and colony counting after incubating for 21 days. All assays were performed in triplicate.

### 4.13. Cytotoxicity against cell lines

The CCK-8 method was applied to determine the cytotoxic effects of LZDT1/LZDT2 on liver hepatocellular cells (HepG2), human neuroblastoma cells (SH-SY5Y), and human embryonic kidney 293 cells (HEK293). For detail, each cell line was cultured to the logarithmic phase as per standard practice, and diluted to 3 × $10^4$ cells/mL by fresh DMEM with 10% fetal bovine serum (FBS). 100 μL diluted cell cultures containing gradient concentrations of LZDT1/LZDT2 (0.00, 1.56, 3.12, 6.25, 12.50, 25.00, 50.00, and 100.00 μg/mL) were planted into each well of the 96-well plates for cell culture. Cells were cultured in the humidified incubator (37 °C and 5% $CO_2$) for 72 h. To determine cell viability, cells in each well were subsequently mixed with 10 μL CCK-8 and incubated for two more hours without light (37 °C, 5% $CO_2$, humidified incubator). The cell viability was characterized by the $OD_{492}$ values of each well as assayed by a TECAN Infinite M200 microplate reader (TECAN, Switzerland). TCA1 was taken as a positive control and DMSO (1%, v/v) was taken as a negative control. Under all assay conditions, the final concentration of DMSO was fixed at 1% (v/v).

### 4.14. Electrostatic complementarity calculation

Electrostatic interactions between proteins and ligands are essential contributors to the binding free energy of protein-ligand complexes. Assessing the electrostatic complementarity (EC) of protein-ligand complexes can provide important insights into why ligands bind and what can be changed to improve binding. Here in the present research, the EC of complexes formed by DprE1 and TCA1 analogs was analyzed using the Flare V3 software. The detail process was conducted based on the method reported by Bauer and Mackey [43,72].

### 4.15. Synthesis and characterization data for LZDT1~LZDT11

Detail information is provided in the Supporting Information (SI).

### 4.16. Statistics

The experimental binding free energy changes ($\Delta\Delta G_{bind\text{-}exp}$) caused by the mutation of each residue were calculated based on corresponding $IC_{50}$ values using eq (1) [51,65,66].

$$\Delta\Delta Gbind - exp = RT\ ln(IC50 - MT\ /\ IC50 - WT) \quad (1)$$

In eq (1), *R* is the ideal gas constant, *T* is the Kelvin temperature, $IC_{50\text{-}MT}$ is the $IC_{50}$ values between mutant DprE1 proteins and test compounds (LZDT1 and TCA1), $IC_{50\text{-}WT}$ is the $IC_{50}$ values between wild-type DprE1 proteins and test compounds (LZDT1 and TCA1).

The inhibition rate (IR) of test compounds against HepG2 cells was calculated using eq (2) [50,73].

$$IR = (ODctrl - ODexp)\ /\ (ODctrl - ODblk) \quad (2)$$

In eq (2), $OD_{ctrl}$ is the OD values of negative control, $OD_{exp}$ is the OD values of test compounds, $OD_{blk}$ is the background OD values of adopted 96-well plate.

## Declaration of competing interest

The authors declare that they have no known competing financial interests or personal relationships that could have appeared to influence the work reported in this paper.

## Acknowledgements

We are grateful to Prof. John Richard Schrock (Emporia State University, USA) for revising this manuscript. We thank Ms. Ruichi Li for her help in optimizing the graphical abstract. This research was supported by the National Natural Science Foundation of China (No. 21503272, 21877124), the General Financial Grant from the China Postdoctoral Science Foundation (No. 2015M572753), and the National Institutes of Health Grant (No. 7R01GM118467-05).

## Appendix A. Supplementary data

Supplementary data to this article can be found online at https://doi.org/10.1016/j.ejmech.2021.113932.

## Author contributions

Y.L.Z., Z.T., H.W.L., J.Y.L., H.Q.D., and B.W. conceived the project. Y.L.Z., Z.T., H.W.L., J.Y.L., and H.Q.D. designed the experiment. J.Y.L., B.W., and Z.T. performed the experiments and prepared the manuscript. Y.L.Z., Z.T., and H.W.L. supervised the study and contributed the reagents and materials. All authors contributed to data analysis.

## References


[1] R. Granich, Is the global tuberculosis control strategy too big to fail? Lancet 392 (2018) 2165.
[2] A. MacNeil, Global epidemiology of tuberculosis and progress toward meeting global targets—worldwide, 2018, Morbid. Mortal. W. 69 (2020) 281–285.
[3] A. Zumla, J. Chakaya, R. Centis, L. D'Ambrosio, P. Mwaba, M. Bates, N. Kapata, T. Nyirenda, D. Chanda, S. Mfinanga, Tuberculosis treatment and management—an update on treatment regimens, trials, new drugs, and adjunct therapies, Lancet Respir. Med. 3 (2015) 220–234.
[4] K.A. Alene, K. Wangdi, A.C. Clements, Impact of the COVID-19 pandemic on tuberculosis control: an overview, Trop. Med. Infect. Dis. 5 (2020) 123.
[5] A.B. Hogan, B.L. Jewell, E. Sherrard-Smith, J.F. Vesga, O.J. Watson, C. Whittaker, A. Hamlet, J.A. Smith, P. Winskill, R. Verity, Potential impact of the COVID-19 pandemic on HIV, tuberculosis, and malaria in low-income and middle-income countries: a modelling study, Lancet Glob. Health 8 (2020) e1132–e1141.
[6] P. Adepoju, Tuberculosis and HIV responses threatened by COVID-19, Lancet HIV 7 (2020) e319–e320.
[7] Q.A. Karim, S.S.A. Karim, COVID-19 affects HIV and tuberculosis care, Science 369 (2020) 366–368.
[8] B.J. Marais, The global tuberculosis situation and the inexorable rise of drug-resistant disease, Adv. Drug Deliv. Rev. 102 (2016) 3–9.
[9] K. Weyer, D. Dennis Falzon, E. Jaramillo, M. Zignol, F. Mirzayev, M. Raviglione, Drug-resistant tuberculosis: what is the situation, what are the needs to roll it back, AMR Control 20 (2017) 60–67.
[10] F. Wu, J. Zhang, F. Song, S. Wang, H. Guo, Q. Wei, H. Dai, X. Chen, X. Xia, X. Liu, Chrysomycin A derivatives for the treatment of multi-drug-resistant tuberculosis, ACS Cent. Sci. 6 (2020) 928–938.
[11] S.B. Herzon, New leads for the treatment of multidrug resistant *Mycobacterium tuberculosis*, ACS Cent. Sci. 6 (2020) 833–835.
[12] E.J. Ashforth, C. Fu, X. Liu, H. Dai, F. Song, H. Guo, L. Zhang, Bioprospecting for antituberculosis leads from microbial metabolites, Nat. Prod. Rep. 27 (2010) 1709–1719.
[13] C. Chen, J. Wang, H. Guo, W. Hou, N. Yang, B. Ren, M. Liu, H. Dai, X. Liu, F. Song, Three antimycobacterial metabolites identified from a marine-derived *Streptomyces* sp. MS100061, Appl. Microbiol. Biotechnol. 97 (2013) 3885–3892.
[14] A. Hotra, P. Ragunathan, P.S. Ng, P. Seankongsuk, A. Harikishore, J.P. Sarathy, S.W. Geok, U. Lakshmanan, P. Sae-Lao, N.P. Kalia, Discovery of a novel Mycobacterial F-ATP synthase inhibitor and its potency in combination with diarylquinolines, Angew. Chem. Int. Ed. 59 (2020) 13295–13304.
[15] Z. Song, Y. Liu, J. Gao, J. Hu, H. He, S. Dai, L. Wang, H. Dai, L. Zhang, F. Song, Antitubercular metabolites from the marine-derived fungus strain *Aspergillus fumigatus* MF029, Nat. Prod. Res. 35 (2019) 2647–2654.
[16] Q. Ye, X. Chai, D. Jiang, L. Yang, C. Shen, X. Zhang, D. Li, D. Cao, T. Hou, Identification of active molecules against *Mycobacterium tuberculosis* through machine learning, Briefings Bioinf. 22 (2021) bbab068.
[17] K. Mikusova, V. Makarov, J. Neres, DprE1—from the discovery to the promising tuberculosis drug target, Curr. Pharmaceut. Des. 20 (2014) 4379–4403.
[18] T. Christophe, M. Jackson, H.K. Jeon, D. Fenistein, M. Contreras-Dominguez, J. Kim, A. Genovesio, J.P. Carralot, F. Ewann, E.H. Kim, High content screening identifies decaprenyl-phosphoribose 2′ epimerase as a target for intracellular antimycobacterial inhibitors, PLoS Pathog. 5 (2009), e100345.
[19] R.V. Chikhale, M.A. Barmade, P.R. Murumkar, M.R. Yadav, Overview of the development of DprE1 inhibitors for combating the menace of tuberculosis, J. Med. Chem. 61 (2018) 8563–8593.
[20] G.S. Kolly, F. Boldrin, C. Sala, N. Dhar, R.C. Hartkoorn, M. Ventura, A. Serafini, J.D. McKinney, R. Manganelli, S.T. Cole, Assessing the essentiality of the decaprenyl-phospho-d-arabinofuranose pathway in *Mycobacterium tuberculosis* using conditional mutants, Mol. Microbiol. 92 (2014) 194–211.
[21] M. Brecik, I. Centárová, R. Mukherjee, G.l.S. Kolly, S. Huszár, A. Bobovská, E.k. Kilacsková, V. Mokosová, Z. Svetlíková, M. Sarkan, DprE1 is a vulnerable tuberculosis drug target due to its cell wall localization, ACS Chem. Biol. 10 (2015) 1631–1636.
[22] S.A. Stanley, S.S. Grant, T. Kawate, N. Iwase, M. Shimizu, C. Wivagg, M. Silvis, E. Kazyanskaya, J. Aquadro, A. Golas, M. Fitzgerald, H. Dai, L. Zhang, H.T. Deborah, Identification of novel inhibitors of *M. tuberculosis* growth using whole cell based high-throughput screening, ACS Chem. Biol. 7 (2012) 1377–1384.
[23] J. Piton, C.S.Y. Foo, S.T. Cole, Structural studies of *Mycobacterium tuberculosis* DprE1 interacting with its inhibitors, Drug Discov. Today 22 (2017) 526–533.
[24] F. Wang, D. Sambandan, R. Halder, J. Wang, S.M. Batt, B. Weinrick, I. Ahmad, P. Yang, Y. Zhang, J. Kim, Identification of a small molecule with activity against drug-resistant and persistent tuberculosis, Proc. Natil. Acad. Sci. U.S.A. 110 (2013) E2510–E2517.
[25] R. Liu, X. Lyu, S.M. Batt, M.H. Hsu, M.B. Harbut, C. Vilchèze, B. Cheng, K. Ajayi, B. Yang, Y. Yang, Determinants of the inhibition of DprE1 and CYP2C9 by antitubercular thiophenes, Angew. Chem. Int. Ed. 56 (2017) 13011–13015.
[26] S.M. Batt, T. Jabeen, V. Bhowruth, L. Quill, P.A. Lund, L. Eggeling, L.J. Alderwick, K. Fütterer, G.S. Besra, Structural basis of inhibition of *Mycobacterium tuberculosis* DprE1 by benzothiazinone inhibitors, Proc. Natil. Acad. Sci. U.S.A. 109 (2012) 11354–11359.
[27] V. Makarov, B. Lechartier, M. Zhang, J. Neres, A.M. van der Sar, S.A. Raadsen, R.C. Hartkoorn, O.B. Ryabova, A. Vocat, L.A. Decosterd, Towards a new combination therapy for tuberculosis with next generation benzothiazinones, EMBO Mol. Med. 6 (2014) 372–383.
[28] J. Neres, F. Pojer, E. Molteni, L.R. Chiarelli, N. Dhar, S. Boy-Röttger, S. Buroni, E. Fullam, G. Degiacomi, A.P. Lucarelli, Structural basis for benzothiazinone-mediated killing of *Mycobacterium tuberculosis*, Sci. Transl. Med. 4 (2012) 150ra121.
[29] H. Li, G. Jogl, Crystal structure of decaprenylphosphoryl-β-D-ribose 2'-epimerase from *Mycobacterium smegmatis*, Proteins: Struct. Funct. Bioinf. 81 (2013) 538–543.
[30] J. Neres, R.C. Hartkoorn, L.R. Chiarelli, R. Gadupudi, M.R. Pasca, G. Mori, A. Venturelli, S. Savina, V. Makarov, G.S. Kolly, 2-Carboxyquinoxalines kill *Mycobacterium tuberculosis* through noncovalent inhibition of DprE1, ACS Chem. Biol. 10 (2015) 705–714.
[31] World Health Organization, The Use of Bedaquiline in the Treatment of Multidrug-Resistant Tuberculosis: Interim Policy Guidance, 2013.
[32] R. Mahajan, Bedaquiline: first FDA-approved tuberculosis drug in 40 years, Int. J. Appl. Basic Med. Res. 3 (2013) 1–2.
[33] K. Hards, J.R. Robson, M. Berney, L. Shaw, D. Bald, A. Koul, K. Andries, G.M. Cook, Bactericidal mode of action of bedaquiline, J. Antimicrob. Chemother. 70 (2015) 2028–2037.
[34] J.K. Martin II, J.P. Sheehan, B.P. Bratton, G.M. Moore, A. Mateus, S.H.J. Li, H. Kim, J.D. Rabinowitz, A. Typas, M.M. Savitski, A dual-mechanism antibiotic kills Gram-negative bacteria and avoids drug resistance, Cell 181 (2020) 1518–1532.
[35] T.T. Talele, The "cyclopropyl fragment" is a versatile player that frequently appears in preclinical/clinical drug molecules, J. Med. Chem. 59 (2016) 8712–8756.
[36] C.J. Suckling, The cyclopropyl group in studies of enzyme mechanism and inhibition, Angew. Chem. Int. Ed. 27 (1988) 537–552.
[37] M. Panda, S. Ramachandran, V. Ramachandran, P.S. Shirude, V. Humnabadkar, K. Nagalapur, S. Sharma, P. Kaur, S. Guptha, A. Narayan, Discovery of pyrazolopyridones as a novel class of noncovalent DprE1 inhibitor with potent anti-mycobacterial activity, J. Med. Chem. 57 (2014) 4761–4771.
[38] C. Trefzer, H. Skovierová, S. Buroni, A. Bobovská, S. Nenci, E. Molteni, F. Pojer, M.R. Pasca, V. Makarov, S.T. Cole, Benzothiazinones are suicide inhibitors of mycobacterial decaprenylphosphoryl-β-d-ribofuranose 2′-oxidase DprE1, J. Am. Chem. Soc. 134 (2012) 912–915.
[39] C. Trefzer, M. Rengifo-Gonzalez, M.J. Hinner, P. Schneider, V. Makarov, S.T. Cole, K. Johnsson, Benzothiazinones: prodrugs that covalently modify the decaprenylphosphoryl-β-D-ribose 2′-epimerase DprE1 of *Mycobacterium tuberculosis*, J. Am. Chem. Soc. 132 (2010) 13663–13665.
[40] C.S.Y. Foo, B. Lechartier, G.S. Kolly, S. Boy-Röttger, J. Neres, J. Rybniker, A. Lupien, C. Sala, J. Piton, S.T. Cole, Characterization of DprE1-mediated benzothiazinone resistance in *Mycobacterium tuberculosis*, Antimicrob. Agents Chemother. 60 (2016) 6451–6459.
[41] V. Makarov, G. Manina, K. Mikusova, U. Möllmann, O. Ryabova, B. Saint-Joanis, N. Dhar, M.R. Pasca, S. Buroni, A.P. Lucarelli, Benzothiazinones kill *Mycobacterium tuberculosis* by blocking arabinan synthesis, Science 324 (2009) 801–804.
[42] M. Adams, T. Kobayashi, J.D. Lawson, M. Saitoh, K. Shimokawa, S.V. Bigi, M.S. Hixon, C.R. Smith, T. Tatamiya, M. Goto, J. Russo, C.E. Grimshaw, S. Swann, Fragment-based drug discovery of potent and selective MKK3/6 inhibitors, Bioorg. Med. Chem. Lett 26 (2016) 1086–1089.
[43] M.R. Bauer, M.D. Mackey, Electrostatic complementarity as a fast and effective tool to optimize binding and selectivity of protein–ligand complexes, J. Med. Chem. 62 (2019) 3036–3050.
[44] W. DeLano, The PyMOL Molecular Graphics System, Schrödinger, LLC, New York, 2010, Version 1.3 r1.
[45] D.A. Case, T.A. Darden, T.E. Chentham III, C.L. Simmerling, J. Wang, R.E. Duke, et al., AMBER 12, University of California, San Francisco, 2012.
[46] W.L. Jorgensen, Theoretical studies of medium effects on conformational equilibria, J. Phys. Chem. 87 (1983) 5304–5314.
[47] J. Wang, R.M. Wolf, J.W. Caldwell, P.A. Kollman, D.A. Case, Development and testing of a general amber force field, J. Comput. Chem. 25 (2004) 1157–1174.
[48] A. Jakalian, D.B. Jack, C.I. Bayly, Fast, efficient generation of high-quality atomic charges. AM1-BCC model: II. Parameterization and validation, J. Comput. Chem. 23 (2002) 1623–1641.
[49] G. Hummer, J.C. Rasaiah, J.P. Noworyta, Water conduction through the hydrophobic channel of a carbon nanotube, Nature 414 (2001) 188–190.
[50] J. Liu, L. Liu, Z. Tian, Y. Li, C. Shi, J. Shi, S. Wei, Y. Zhao, C. Zhang, B. Bai, In silico discovery of a small molecule suppressing lung carcinoma A549 cells proliferation and inducing autophagy via mTOR pathway inhibition, Mol. Pharm. 15 (2018) 5427–5436.
[51] Z. Tian, Y. Li, Y. Xing, R. Li, J. Liu, Structural insights into two representative conformations of the complex formed by *Grapholita molesta* (Busck) pheromone binding protein 2 and Z-8-dodecenyl acetate, J. Agric. Food Chem. 67 (2019) 4425–4434.
[52] H.J. Berendsen, J.v. Postma, W.F. van Gunsteren, A. DiNola, J. Haak, Molecular dynamics with coupling to an external bath, J. Chem. Phys. 81 (1984) 3684–3690.
[53] Z. Tian, Y. Li, T. Zhou, X. Ye, R. Li, J. Liu, Structure dynamics reveal key residues essential for the sense of 1-dodecanol by *Cydia pomonella* pheromone binding protein 2 (CpomPBP2), Pest Manag. Sci. 76 (2020) 3667–3675.
[54] Z. Tian, J. Liu, Y. Zhang, Key residues involved in the interaction between *Cydia pomonella* pheromone binding protein 1 (CpomPBP1) and Codlemone, J. Agric.

Food Chem. 64 (2016) 7994–8001.
[55] Z. Tian, J. Liu, Y. Zhang, Structural insights into *Cydia pomonella* pheromone binding protein 2 mediated prediction of potentially active semiochemicals, Sci. Rep. 6 (2016) 22336.
[56] J. Liu, Z. Tian, Y. Zhang, Structure-based discovery of potentially active semiochemicals for *Cydia pomonella* (L.), Sci. Rep. 6 (2016) 34600.
[57] T. Hou, J. Wang, Y. Li, W. Wang, Assessing the performance of the molecular mechanics/Poisson Boltzmann surface area and molecular mechanics/generalized Born surface area methods. II. The accuracy of ranking poses generated from docking, J. Comput. Chem. 32 (2011) 866–877.
[58] J. Kottalam, D. Case, Langevin modes of macromolecules: applications to crambin and DNA hexamers, Biopolymers: Orig. Res. Biomol. 29 (1990) 1409–1421.
[59] J. Liu, Z. Tian, N. Zhou, X. Liu, C. Liao, B. Lei, J. Li, S. Zhang, H. Chen, Targeting the apoptotic Mcl-1-PUMA interface with a dual-acting compound, Oncotarget 8 (2017) 54236–54242.
[60] A. Metz, C. Pfleger, H. Kopitz, S. Pfeiffer-Marek, K.H. Baringhaus, H. Gohlke, Hot spots and transient pockets: predicting the determinants of small-molecule binding to a protein–protein interface, J. Chem. Inf. Model. 52 (2012) 120–133.
[61] H. Gohlke, C. Kiel, D.A. Case, Insights into protein–protein binding by binding free energy calculation and free energy decomposition for the Ras–Raf and Ras–RalGDS complexes, J. Mol. Biol. 330 (2003) 891–913.
[62] K. Raha, A.J. van der Vaart, K.E. Riley, M.B. Peters, L.M. Westerhoff, H. Kim, K.M. Merz, Pairwise decomposition of residue interaction energies using semiempirical quantum mechanical methods in studies of protein– ligand interaction, J. Am. Chem. Soc. 127 (2005) 6583–6594.
[63] P.A. Kollman, I. Massova, C. Reyes, B. Kuhn, S. Huo, L. Chong, M. Lee, T. Lee, Y. Duan, W. Wang, Calculating structures and free energies of complex molecules: combining molecular mechanics and continuum models, Accounts Chem. Res. 33 (2000) 889–897.
[64] B.R. Miller, T.D. McGee, J.M. Swails, N. Homeyer, H. Gohlke, A.E. Roitberg, MMPBSA.py: an efficient program for end-state free energy calculations, J. Chem. Theor. Comput. 8 (2012) 3314–3321.
[65] I.S. Moreira, P.A. Fernandes, M.J. Ramos, Computational alanine scanning mutagenesis—an improved methodological approach, J. Comput. Chem. 28 (2007) 644–654.
[66] J. Liu, Y. Li, Z. Tian, H. Sun, X.e. Chen, S. Zheng, Y. Zhang, Identification of key residues associated with the interaction between *Plutella xylostella* sigma-class glutathione S-transferase and the inhibitor S-hexyl glutathione, J. Agric. Food Chem. 66 (2018) 10169–10178.
[67] Enamine. https://enamine.net/.
[68] ChemDiv. https://www.chemdiv.com/.
[69] G.F. Hao, F. Wang, H. Li, X.L. Zhu, W.-C. Yang, L.S. Huang, J.W. Wu, E.A. Berry, G.F. Yang, Computational discovery of picomolar Qo site inhibitors of cytochrome bc 1 complex, J. Am. Chem. Soc. 134 (2012) 11168–11176.
[70] G.F. Hao, W. Jiang, Y.N. Ye, F.X. Wu, X.L. Zhu, F.B. Guo, G.F. Yang, ACFIS: a web server for fragment-based drug discovery, Nucleic Acids Res. 44 (2016) W550–W556.
[71] J.G. Vinter, Extended electron distributions applied to the molecular mechanics of some intermolecular interactions, J. Comput. Aided Mol. Des. 8 (1994) 653–668.
[72] Flare V3, Cresset®, Litlington, Cambridgeshire, UK. http://www.cresset-group.com/flare/.
[73] X. Wang, S. Wei, Y. Zhao, C. Shi, P. Liu, C. Zhang, Y. Lei, B. Zhang, B. Bai, Y. Huang, Anti-proliferation of breast cancer cells with itraconazole: Hedgehog pathway inhibition induces apoptosis and autophagic cell death, Cancer Lett. 385 (2017) 128–136.